Li et al. *NPG Asia Materials* (2018) 10: 522-532
DOI 10.1038/s41427-018-0050-5

NPG Asia Materials

ARTICLE Open Access

Observation of superconductivity in structure-selected Ti_2O_3 thin films

Yangyang Li[1,2], Yakui Weng[3], Junjie Zhang[3], Junfeng Ding[1,4], Yihan Zhu[5], Qingxiao Wang[1,6], Yang Yang[7], Yingchun Cheng[8], Qiang Zhang[1], Peng Li[1], Jiadan Lin[9], Wei Chen[9], Yu Han[5], Xixiang Zhang[1], Lang Chen[10], Xi Chen[11], Jingsheng Chen[2], Shuai Dong[3], Xianhui Chen[12] and Tom Wu[1,13]

Abstract

The search for new superconductors capable of carrying loss-free current has been a research theme in condensed matter physics for the past decade. Among superconducting compounds, titanates have not been pursued as much as Cu^{2+} ($3d^9$) (cuprate) and Fe^{2+} ($3d^6$) (pnictide) compounds. Particularly, Ti^{3+}-based compounds or electron systems with a special $3d^1$ filling are thought to be promising candidates as high-T_C superconductors, but there has been no report on such pure Ti^{3+}-based superconducting titanates. With the advent of thin-film growth technology, stabilizing new structural phases in single-crystalline thin films is a promising strategy to realize physical properties that are absent in the bulk counterparts. Herein, we report the discovery of unexpected superconductivity in orthorhombic-structured thin films of Ti_2O_3, a $3d^1$ electron system, which is in strong contrast to the conventional semiconducting corundum-structured Ti_2O_3. This is the first report of superconductivity in a titanate with a pure $3d^1$ electron configuration. Superconductivity at 8 K was observed in the orthorhombic Ti_2O_3 films. Leveraging the strong structure-property correlation in transition-metal oxides, our discovery introduces a previously unrecognized route for inducing emergent superconductivity in a newly stabilized polymorph phase in epitaxial thin films.

Introduction

Exploring structure-property correlations is a frontier of material science, which enables researchers to understand and harness the emergent properties of advanced materials. Functional oxides have attracted attention due to their strong structure-property correlation.[1–6] For example, enhanced multiferroic properties have been discovered in epitaxial-stabilized tetragonal $BiFeO_3$[7] and hexagonal $TbMnO_3$ films,[8] and these structures are absent in the bulk counterparts. Superconductors have zero electrical resistance and magnetic flux expulsion below certain critical temperatures. Motivated by both scientific curiosity and application demands, extensive efforts have been devoted to seeking new, high-T_C superconductors and exploring the origin of superconductivity. However, emergent superconductivity in thin films with newly stabilized polymorph phases has not been reported. Recently, nanosized, trigonal corundum Ti_2O_3 phase has attracted much attention owing to its narrow bandgap and efficient photothermal effect.[9] Here, we report the discovery of a strong structure-property correlation in Ti_2O_3 polymorphs; i.e., superconductivity emerges in orthorhombic Ti_2O_3 films epitaxially stabilized on sapphire substrates, while the trigonal bulk phase is semiconducting.

Most milestones in superconductivity research have been set by the discoveries of new materials such as cuprates[10,11] and Fe-based superconductors.[12–15] In addition, there are some notable transition-metal-oxide superconductors, such as tungsten bronzes with T_C values up to 6 K.[16,17] Within the $3d$-transition-metal series, Ti^3

Correspondence: Shuai Dong (sdong@seu.edu.cn) or Tom Wu (tom.wu@unsw.edu.au)
[1]Physical Science and Engineering Division, King Abdullah University of Science and Technology (KAUST), Thuwal 23955-6900, Saudi Arabia
[2]Department of Materials Science and Engineering, National University of Singapore, Singapore 117575, Singapore
Full list of author information is available at the end of the article.
These authors contributed equally: Yakui Weng, Junjie Zhang

$^{+}$-based compounds are predicted to be promising candidates for high-T_C superconductors as a result of their special filling ($3d^1$ and $S = 1/2$),[18] but superconducting titanates have been limited to materials like electron-doped $SrTiO_3$ (T_C≈0.41 K),[19] non-stoichiometric titanium monoxide TiO_x ($T_C \leq 2.3$ K)[20,21] and ternary oxide Li-Ti-O (T_C≈14 K).[22–24] Recently, interest in superconducting titanate thin films has resurged, and superconductivity in TiO,[25] γ-Ti_3O_5,[26,27] and Ti_4O_7[26,27] was reported. It is important to note that these titanates feature Ti^{2+} or mixed (Ti^{3+}/Ti^{4+}) valence states, and there has been no report of superconductivity in a "pure" Ti^{3+} ($3d^1$) system.

Little progress has been made over the past several decades in the search for binary-oxide superconductors, which might possess attractive characteristics such as structural simplicity, high tenability and environmental stability. Among the few superconducting binary oxides reported to date, monoxide NbO exhibits a very low T_C of 1.38 K.[28] Among sesquioxides, Zn-doped and Sn-doped In_2O_3 were reported to be superconducting at 3.3 K[29] and 4 K,[30] respectively. The recent advent of thin film synthesis techniques offers a new route towards achieving superconductivity at high transition temperatures in epitaxial films and heterostructures. For example, in one pioneering work, superconductivity was reported to be above 100 K in single-layer FeSe films,[31] while bulk FeSe shows superconductivity below 8 K.[32] Inspired by these discoveries, we postulate that investigating titanites, particularly Ti^{3+}-containing Ti_2O_3, in a thin film form might open a new door in the search for new oxide superconductors.

In this work, we report the discovery of superconductivity in newly stabilized, epitaxial, orthorhombic-structured Ti_2O_3 thin films grown on α-Al_2O_3 substrates, which demonstrates the strong structure-property correlation in such strongly correlated electron systems. Although six different lattice variants of Ti_2O_3 were predicted, i.e., corundum, Rh_2O_3 (II)-type, perovskite, post-perovskite, α-Gd_2S_3-type and Th_2S_3-type, only corundum and Th_2S_3-like types have been reported experimentally.[33] Surprisingly, we found that the structure of Ti_2O_3 thin films can be selected by tuning the growth conditions; particularly, a hitherto unreported orthorhombic Rh_2O_3-like structure was discovered. Furthermore, although the conventional corundum-type Ti_2O_3 is a regular, narrow-bandgap semiconductor, the orthorhombic thin films are a new oxide superconductor with a T_C of 8 K. In fact, this is, to our knowledge, the first report demonstrating emergent superconductivity in thin films of a certain material while absent in the bulk counterpart. Our discovery offers a new route to inducing superconductivity in artificial epitaxial thin films and heterostructures by modifying their polymorph crystalline structures.

Materials and methods

Fabrication of Ti_2O_3 thin films

Ti_2O_3 films with a thickness range of 40–280 nm were deposited on (0001) sapphire substrates with a size of $5 \times 5 \times 0.5$ mm^3 using pulsed laser deposition (PLD). A corundum-phase Ti_2O_3 target (Sigma-Aldrich, 99.99%) was used. Before deposition, the pressure of the PLD chamber was lower than 3.0×10^{-9} Torr. The deposition was performed at temperatures from 500 to 900 °C with a 248 nm laser (KrF, Coherent Inc.). The energy density of the laser on the target was varied from 2 J/cm^2 to 3 J/cm^2. The distance between the target and substrates was fixed at 5.6 cm. More synthesis details are given in Table S1.

X-ray diffraction (XRD)

X-ray diffraction patterns were recorded using a Bruker D8 ADVANCE diffractometer (used for powder samples) and Bruker D8 DISCOVER high-resolution diffractometer (used for thin film samples) operated at 40 kV/40 mA and 35 kV/50 mA, respectively. Both diffractometers were equipped with Cu Kα radiation source and LynxEye detector.

Raman spectroscopy

Raman measurements were performed with a confocal micro-Raman system (Horiba Aramis/Jobin Yvon HR800) at ambient conditions. The wavelength of the excitation solid-state laser is 473 nm. The laser beam was focused on thin film samples using a ×100 objective lens (×50 objective for powder samples) with a numeric aperture (NA) of 0.90, and the spot size was approximately 1 μm. A typical laser power of 0.5 mW was used to avoid sample heating. The spectra were calibrated using a standard silicon sample.

X-ray photoelectron spectroscopy (XPS)

XPS measurements were carried out on a custom-built ultra-high-vacuum system with a Mg Kα (1253.6 eV) excitation source. The vacuum of the analysis chamber was approximately 2×10^{-9} Torr, and the spectrum was calibrated according to the O 1*s* XPS spectra (530.3 eV) before the first experiment on the Ti_2O_3-LT sample. Before the XPS experiments, the samples were sputtered for 27 min to remove contaminated surface layers.

Transmission electron microscopy

A focused ion beam (FEI Helios 400S) was used to prepare the cross-section samples for the S/TEM analyses. A protecting Pt layer was deposited on the top of the Ti_2O_3 thin film. S/TEM lamella with a thickness of ~100 nm was transferred to a half-moon FIB grid by an in situ lift-out method, followed by low-energy Ar-ion cleaning in a Fischione Nano Mill 1040. The damaged surface layer was removed, and the final thickness of the sample was

~20 nm. The cross-sections of Pt/Ti_2O_3/sapphire structures were characterized using a scanning transmission electron microscope (Titan Mono-Probe Cs, FEI). Electron diffraction patterns were obtained with a TitanST electron microscope operated at 300 kV. HAADF-STEM images were collected with an aberration-corrected Mono-Probe Cs scanning transmission electron microscope (Titan, FEI) operated at 300 kV using a convergence semi-angle of 21 mrad. The inner collection semi-angle of the HAADF was 70 mrad.

Transport and magnetic measurements

The electrical transport and magnetic measurements were performed using a Quantum Design physical property measurement system (PPMS) and a Quantum Design superconducting quantum interference device, respectively. For the transport measurements, electrodes with 30 nm of titanium and 100 nm of platinum with a size of $0.5 \times 0.5\ mm^2$ were deposited by sputtering. Gold wires were used to connect the samples to the PPMS puck. In the magnetic measurements, a quartz holder and a straw were used to support the sample when the magnetic field was parallel and vertical to the film surface, respectively. Data were recorded at 10 Oe during warming after being zero-field cooled from 300 to 2 K. A ceramic tweezer was used to handle the samples during all measurements.

First-principles calculations

The electronic structure calculations were performed based on a generalized gradient approximation (GGA) with the Perdew-Burke-Ernzerhof-revised (PBEsol) function,[34] as implemented in the Vienna ab initio Simulation Package.[35,36] Two types of structural relaxations were performed: (1) full relaxation of lattice constants and inner atomic positions and (2) relaxation of inner atomic positions with only fixed experimental lattice constants. The Hubbard U was applied to Ti d orbitals. In addition, hybrid functional calculations based on the Heyd-Scuseria-Ernzerhof exchange[37] were also performed to correctly describe the bandgaps. Nonmagnetic states were considered. The phonon structure and e-ph coupling were calculated using the PWSCF program of the Quantum-ESPRESSO distribution based on density function perturbation theory.[38]

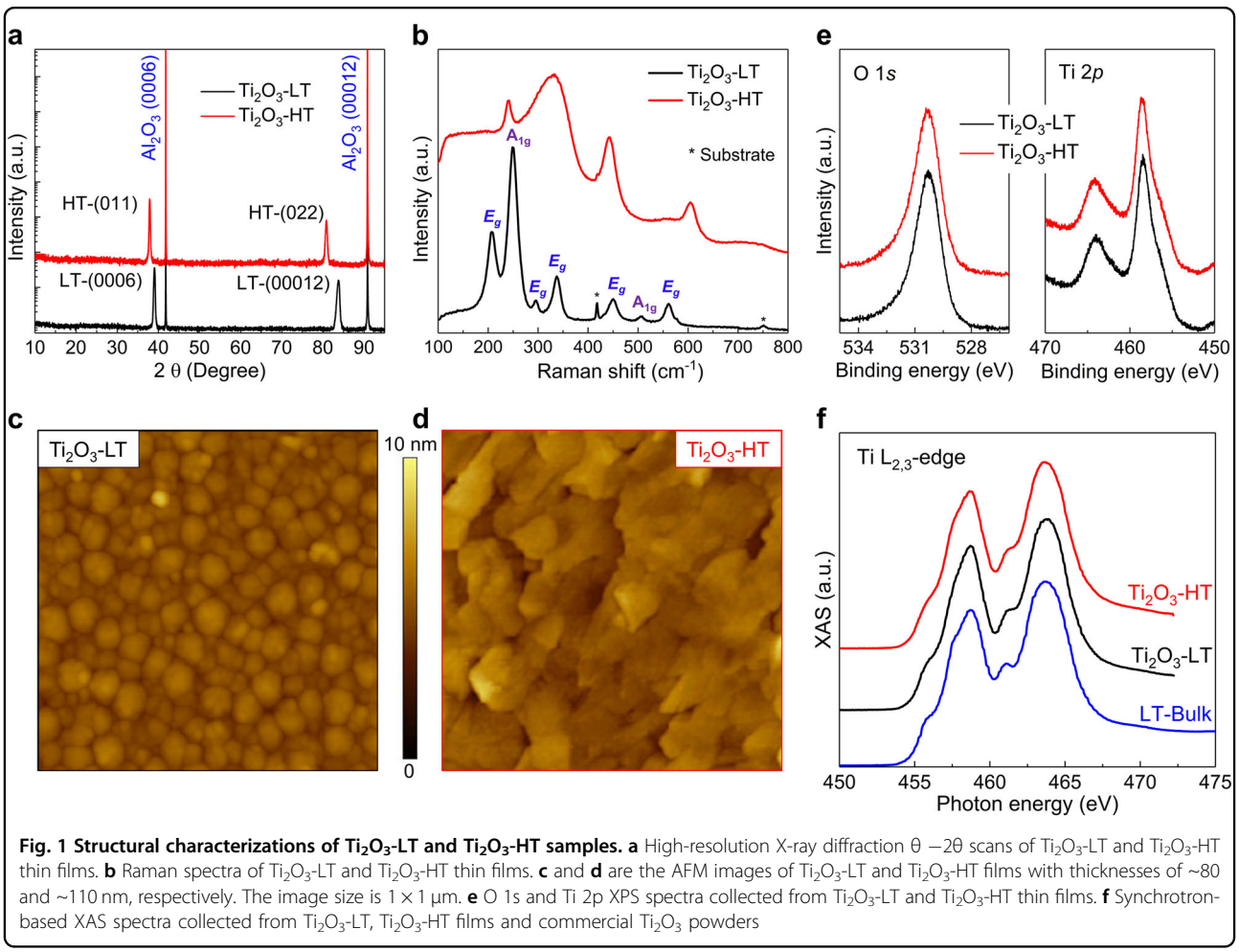

Fig. 1 Structural characterizations of Ti_2O_3-LT and Ti_2O_3-HT samples. a High-resolution X-ray diffraction θ −2θ scans of Ti_2O_3-LT and Ti_2O_3-HT thin films. **b** Raman spectra of Ti_2O_3-LT and Ti_2O_3-HT thin films. **c** and **d** are the AFM images of Ti_2O_3-LT and Ti_2O_3-HT films with thicknesses of ~80 and ~110 nm, respectively. The image size is 1 × 1 μm. **e** O 1s and Ti 2p XPS spectra collected from Ti_2O_3-LT and Ti_2O_3-HT thin films. **f** Synchrotron-based XAS spectra collected from Ti_2O_3-LT, Ti_2O_3-HT films and commercial Ti_2O_3 powders

Results and discussion

Thin-film deposition and structural characterizations

The epitaxial Ti_2O_3 thin films were deposited on α-Al_2O_3 (0001) substrates in a high vacuum (<3.0×10^{-9} Torr) using PLD. Experimental details are provided in the Supplementary Materials. XRD was used to examine the crystal structure and phase of the as-deposited films. The diffraction patterns of Ti_2O_3 thin films grown at 600 °C (sample denoted as Ti_2O_3-LT) and 900 °C (sample denoted as Ti_2O_3-HT) on α-Al_2O_3 substrates are shown in Fig. 1a and Supplementary Figure S1. Cross-sectional transmission electron microscopy (TEM) was used to determine and calibrate the film thickness in this work (Supplementary Figure S2). Apart from the substrate peak, the peaks at 39.06° and 83.78° in the 600 °C grown sample (Ti_2O_3-LT) agree well with the (0006) and (00012) planes, respectively, of the known corundum (trigonal) structure of Ti_2O_3 ($R\bar{3}c$ space group, #167, a = b = 5.15`Å, c = 13.61 Å). Surprisingly, the XRD peaks of the 900 °C grown sample (Ti_2O_3-HT) are located at different locations of 37.90° and 80.86°, indicating a phase different from that of Ti_2O_3-LT. Note that based on the XRD peak positions, the Ti_2O_3-HT phase can be well distinguished from the TiO phase.[25]

Furthermore, we carefully explored the PLD synthesis parameters and determined the conditions for growing Ti_2O_3-LT and Ti_2O_3-HT phases (Supplementary Figure S3). We should note here that both Ti_2O_3-LT and Ti_2O_3-HT thin films are stable. No change was observed in their appearance and structure after being stored under ambient conditions for over half a year (Supplementary Figure S4).

As shown in Fig. 1b, the Raman modes observed in the Ti_2O_3-LT film are consistent with the D_{34} point-group symmetry of the corundum structure (Supplementary Figure S4).[39] On the other hand, for the as-deposited Ti_2O_3-HT film, only four peaks were observed, indicating a different lattice structure and higher lattice symmetry. Raman data also allow us to exclude the existence of titanium oxides other than Ti_2O_3. Specifically, the comparison of the Raman spectra of Ti_4O_7 and Ti_2O_3-HT (Supplementary Figure S5) reveals the absence of any Ti_4O_7 phase in our samples.

Atomic force microscopy (AFM) was used to investigate the surface morphology of Ti_2O_3 films, and in an area of 1 μm × 1 μm, Ti_2O_3-LT and Ti_2O_3-HT have similar surface roughnesses of ~0.45 and ~0.40 nm, respectively. However, as shown in Fig. 1c, d, their morphologies are quite different, which reflects their different crystalline structures.

Figure 1e presents the O 1*s* and Ti 2*p* XPS spectra of these Ti_2O_3 thin films. Ti_2O_3-LT and Ti_2O_3-HT films show almost identical XPS spectra, indicating that their Ti ions share the same valence state. Furthermore, the positions of the XPS peaks (464.1 eV and 458.5 eV for Ti $2p_{1/2}$ and Ti $2p_{3/2}$, respectively) are consistent with those of corundum Ti_2O_3 single crystals,[40,41] indicating a dominant Ti valence state of 3+. Note that the XPS spectra are inconsistent with that of Ti_3O_5 (mixed Ti^{3+} and Ti^{4+}).[42]

Finally, electron energy loss spectroscopy[43,44] and synchrotron-based X-ray absorption spectroscopy (XAS)[43] were used to further confirm the valence state of Ti^{3+} in both phases. As shown in Fig. 1f, the XAS spectra collected from Ti_2O_3-LT and Ti_2O_3-HT films are identical and consistent with that of the standard corundum Ti_2O_3 bulk.[45] Meanwhile, the Ti^{3+} valence state was confirmed by XPS and XAS in the Ti_2O_3-HT sample, which also reveals a difference from that of previously reported TiO,[25] Ti_3O_5 and Ti_4O_7.[27]

Microstructural characterization of Ti2O3-LT and Ti2O3-HT thin films

The discovery of this new Ti_2O_3-HT phase motivated us to carry out in-depth TEM experiments. High-angle annular dark field scanning transmission electron microscopy (HAADF-STEM) images were collected at the interfaces of Ti_2O_3-LT/Al_2O_3 and Ti_2O_3-HT/Al_2O_3. We should note here that there are thin (2–3 nm) transition layers at the interfaces. These transition layers were also observed in some similar cases in previous reports, such as epitaxial TiO[25] and MgB_2[46] films on Al_2O_3. They can be regarded as buffer layers in the epitaxial growth.[47–49] The transition layer observed at the Ti_2O_3/Al_2O_3 interface may not have the stoichiometric composition of Ti_2O_3 due to oxygen diffusion during the film-growth process.[46] However, determining the composition and structure of this intermediate layer is outside the scope of this work.

The HAADF-STEM images taken from two different zone axes (Fig. 2a, e) indicate that the epitaxial relationship between Ti_2O_3-LT and α-Al_2O_3 is $[11\bar{2}0]$ Ti_2O_3-LT‖$[11\bar{2}0]$ α-Al_2O_3 and $[10\bar{1}0]$ Ti_2O_3-LT‖$[10\bar{1}0]$ α-Al_2O_3. Fast Fourier transform (FFT) patterns, obtained from the Ti_2O_3-LT film, are shown as the insets of Fig. 2a, e, which are consistent with the simulated electron diffraction data (Supplementary Figure S6). The inverse FFT (IFFT) images in Fig. 2b, f also confirm the corundum structure of Ti_2O_3-LT.

The HAADF-STEM images of the Ti_2O_3-HT/Al_2O_3 sample, as shown in Fig. 2c, g, suggest a structure that is different from that of corundum Ti_2O_3-LT. Close-up views of the film and substrate lattices are shown in the IFFT images in Fig. 2d, h. In fact, the structure of Ti_2O_3-HT can be reconstructed from that of Ti_2O_3-LT (Supplementary Figure S7). The unit cells of Ti_2O_3-LT ($R\bar{3}c$ space group, #167) and Ti_2O_3-HT (*Immm* space group, #71) are shown as insets in Fig. 2e, g, respectively.

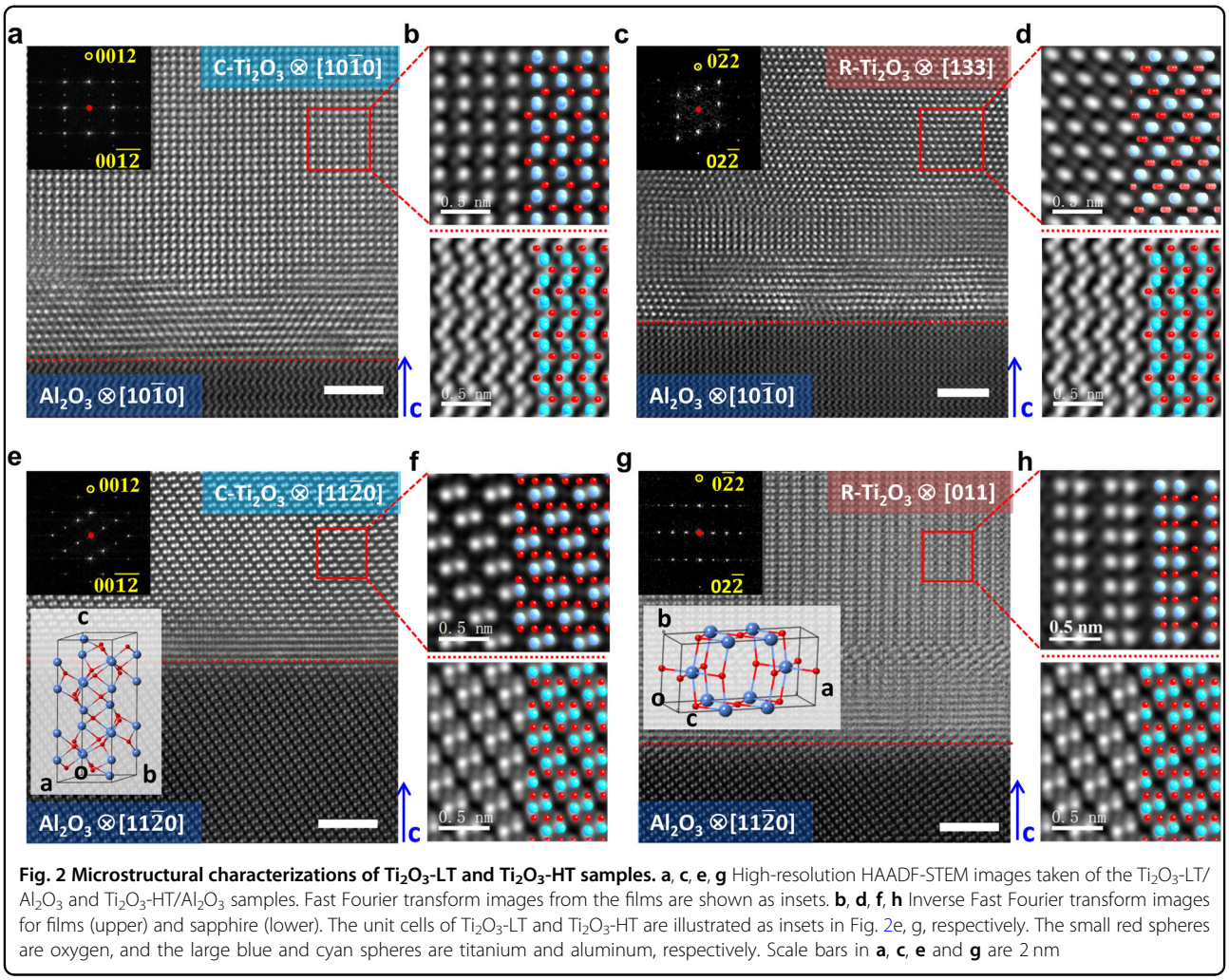

Fig. 2 Microstructural characterizations of Ti_2O_3-LT and Ti_2O_3-HT samples. a, **c**, **e**, **g** High-resolution HAADF-STEM images taken of the Ti_2O_3-LT/Al_2O_3 and Ti_2O_3-HT/Al_2O_3 samples. Fast Fourier transform images from the films are shown as insets. **b**, **d**, **f**, **h** Inverse Fast Fourier transform images for films (upper) and sapphire (lower). The unit cells of Ti_2O_3-LT and Ti_2O_3-HT are illustrated as insets in Fig. 2e, g, respectively. The small red spheres are oxygen, and the large blue and cyan spheres are titanium and aluminum, respectively. Scale bars in **a**, **c**, **e** and **g** are 2 nm

The unit cell parameters of Ti_2O_3-HT are a = 9.385 Å, b = 4.422 Å, and c = 2.809 Å, and a structural comparison with α-Al_2O_3 and Ti_2O_3-LT is given in Fig. 3. Excellent agreement was obtained between the experimental HAADF-STEM images and the projections of the reconstructed structure, as shown in Fig. 2d, h (Supplementary Figure S8). Furthermore, as shown in Supplementary Figure S9, the selected area electron diffraction (SAED) patterns collected from Ti_2O_3-HT/Al_2O_3 are consistent with the simulated results. Finally, the epitaxial relationship between Ti_2O_3-HT and α-Al_2O_3 is confirmed to be [133] Ti_2O_3-HT‖[10$\bar{1}$0] α-Al_2O_3 or [011] Ti_2O_3-HT‖[11$\bar{2}$0] α-Al_2O_3, as shown in Fig. 2c, g, respectively. Supplementary Figure S10 schematically illustrates the in-plane epitaxial relationship between the film and α-Al_2O_3 substrate. The in-plane lattice mismatch between Ti_2O_3-LT and α-Al_2O_3 is approximately 8.4%, while that between Ti_2O_3-HT and α-Al_2O_3 is approximately 2.2 and 5.4% along [011] Ti_2O_3-HT and [100] Ti_2O_3-HT, respectively. When the PLD growth temperature is higher (900 °C), the Ti and O atoms have higher kinetic energies to rearrange themselves into the orthorhombic Ti_2O_3-HT phase to achieve a smaller mismatch with the substrate.

Superconductivity observed in Ti2O3-HT thin films

A metal-insulator transition (Supplementary Figure S11) was found for the Ti_2O_3-HT samples at approximately 370 K, which is much lower than that reported for the corundum-structured Ti_2O_3 (500 K).[50] Hall effect measurements on the Ti_2O_3-LT and Ti_2O_3-HT thin films are shown in Supplementary Figure S12. Ti_2O_3-LT is a p-type semiconductor, which is consistent with previous work,[51] whereas Ti_2O_3-HT is an *n*-type semiconductor. More importantly, the carrier concentration of Ti_2O_3-HT is on the scale of $10^{22}/cm^3$, approximately one order of magnitude higher than that of Ti_2O_3-LT, which is the same order as that of normal metal.[52]

The most important discovery is that the Ti_2O_3-HT samples were superconducting at low temperatures (Fig. 4a), while the Ti_2O_3-LT samples remained

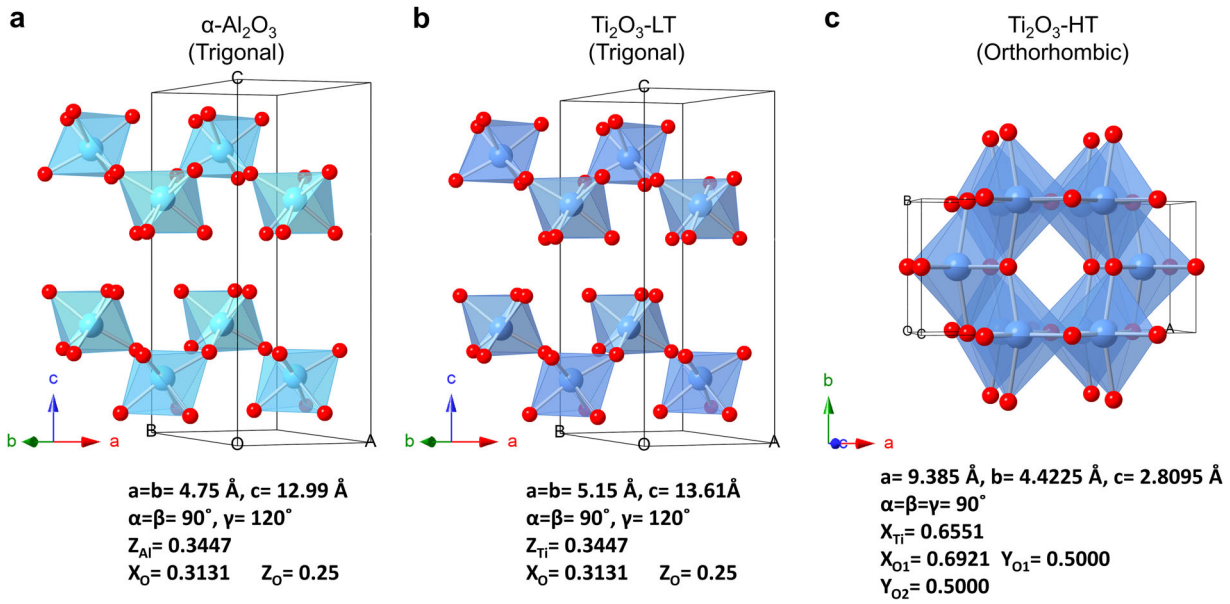

Fig. 3 Crystal structures of (**a**) α-Al_2O_3, (**b**) Ti_2O_3-LT and (**c**) Ti_2O_3-HT. Small red spheres are oxygen. Colorful polyhedra represent bicapped-trigonal prisms enclosing the metal cations

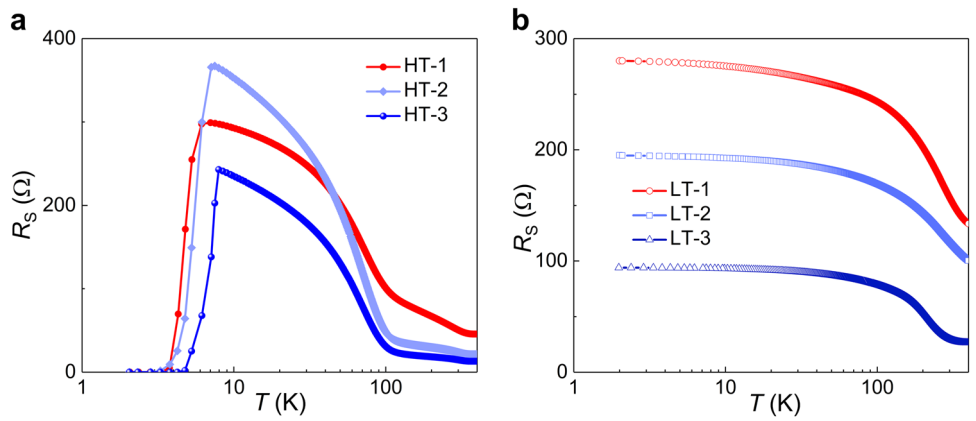

Fig. 4 Electrical transport property of the Ti_2O_3-HT and Ti_2O_3-LT samples. a and **b** are the temperature-dependent sheet resistance measured on the Ti_2O_3-HT and Ti_2O_3-LT films, respectively. No zero-resistance state was observed on Ti_2O_3-LT, while all the Ti_2O_3-HT samples showed superconductivity. Detailed growth conditions for all samples are listed in Table S1

semiconducting (Fig. 4b). One unique property of the superconducting samples of Ti2O3 is the semiconducting transport observed in their high-temperature normal state, which is different from the behavior of common superconductor. In addition to the metal-insulator transition at ~370 K in Ti_2O_3-HT, a semiconductor-semiconductor transition (SST) was observed at ~110 K. A similar SST was observed in $Mg[Ti_2]O_4$,[53] which is also a Ti^{3+} system. The SST in $Mg[Ti_2]O_4$ was believed to be a result of Ti-Ti dimerization instability, and the double-well Ti-Ti bond potential at the crossover changes from localized to itinerant electronic behavior.[53] Most likely, the existence of superconductivity in the $3d^1$ system of Ti_2O_3 is related to the semiconducting normal state and SST, which warrants further investigation.

To exclude the possibility of superconductivity exclusively existing in the intermediate layer and to confirm its bulk nature, we studied the thickness dependence of the superconductivity in the orthorhombic Ti_2O_3-HT samples. Ti_2O_3-HT phase films were grown on α-Al_2O_3 (0001) substrates with thicknesses from ~10 to ~280 nm. As shown in Fig. 5a, we found that the critical transition temperature (Tc: onset) increases with the thickness and saturates at approximately 8 K when the

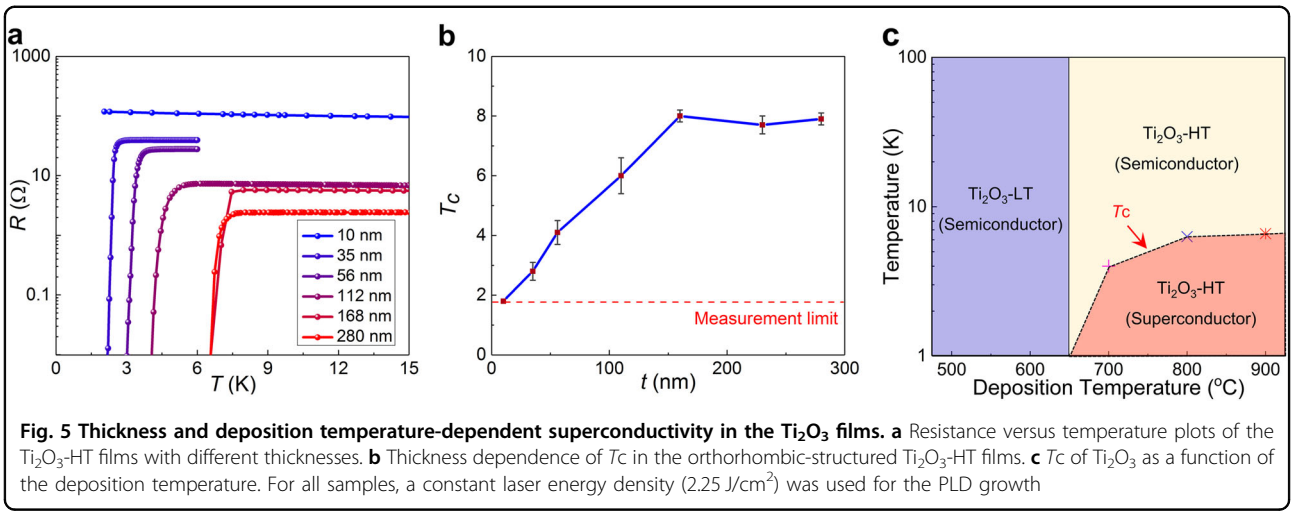

Fig. 5 Thickness and deposition temperature-dependent superconductivity in the Ti_2O_3 films. a Resistance versus temperature plots of the Ti_2O_3-HT films with different thicknesses. **b** Thickness dependence of *Tc* in the orthorhombic-structured Ti_2O_3-HT films. **c** *Tc* of Ti_2O_3 as a function of the deposition temperature. For all samples, a constant laser energy density (2.25 J/cm^2) was used for the PLD growth

thickness is larger than 150 nm (Fig. 5b). When the sample thickness decreases to 10 nm, no superconductivity is observed above 1.8 K (the lowest measurement temperature). In addition to the thickness, the growth temperature is another important factor influencing the Tc of the orthorhombic-structured Ti_2O_3 samples. As shown in Table S1 and Supplementary Figure S13, samples (with the same thickness) deposited at lower temperatures exhibit lower Tc values, which could be a result of their lower degree of crystallinity. In fact, as summarized in Fig. 5c, the PLD growth temperature is the most critical factor determining the phase and superconductivity in Ti_2O_3 samples.

As shown in Fig. 6a, $T_C \approx 8$ K was obtained for Ti_2O_3-HT (sample HT-3 with a thickness of 168 nm), which to our knowledge is the highest T_C ever observed in binary-oxide superconductors. Figure 6b shows that a magnetic field can suppress the superconducting transition temperature of Ti_2O_3-HT. These behaviors were also observed in Ti_2O_3-HT films grown on other types of substrates (Supplementary Figure S14), which indicates that the superconductivity is an intrinsic property of the orthorhombic polymorph of Ti_2O_3. The contour plot shown in Fig. 6c summarizes the variation in the sample resistance as a function of the magnetic field and temperature, showing a phase diagram with a sharp phase boundary between the superconducting and semiconducting regimes.

As shown in Fig. 6d, the critical field, H_C, increased with the decreasing temperature. Below 4 K, the critical field was larger than 9 T. In Fig. 6e, the critical transition fields at different temperatures are fitted to the Ginzburg-Landau (GL) equation:[54] $H_{c2}(T) = H_{c2}(0)\ (1-t^2)/(1+t^2)$, where t denotes a reduced temperature, T/T_c. From the fitting, the upper critical field at zero temperature was estimated to be 21.9 T and the critical temperature to be 8.4 K.

The superconductivity was further confirmed by measuring the diamagnetic property of the Ti_2O_3-HT samples. As shown in Fig. 6f, the magnetization appears saturated at low temperatures, and the superconducting volume fraction is estimated to be more than 99% at 2 K (Supplementary Figure S15), indicating the clear bulk nature of the observed superconductivity. The smaller T_C observed in the magnetization measurement suggests that the superconductivity between 6 and 8 K could be filamentary. In addition, the broadened transition shown in Fig. 6f may imply the existence of some defects that formed during the film deposition.

Theoretical calculations

The physical properties of both Ti_2O_3 phases were further elucidated using density functional theory (DFT) calculations. More details of the DFT calculations can be found in the Supplementary Materials. The electronic structures of Ti_2O_3-LT and Ti_2O_3-HT are shown in Fig. 7a, b, respectively. To simulate the experimental conditions, we adopted the experimental lattice constants and relaxed the atomic positions based on the generalized gradient approximation with Hubbard U (GGA+U). However, as shown in Fig. 7c, the GGA+U calculations led to metallic states for both Ti_2O_3-LT and Ti_2O_3-HT (except in the large U limit for Ti_2O_3-LT), which was different from the experimental semiconducting results. Therefore, newly developed hybrid functional calculations were employed to recalculate the electronic structures based on the GGA+U relaxed structures. As shown in Fig. 7a, b, both Ti_2O_3-LT and Ti_2O_3-HT were predicted to be semiconductors with very narrow bandgaps close to the experimental values (0.108 eV and 0.124 eV, respectively, estimated from the optical absorption data in Supplementary Figure S16). As expected, both the highest valence band and lowest conducting band around the

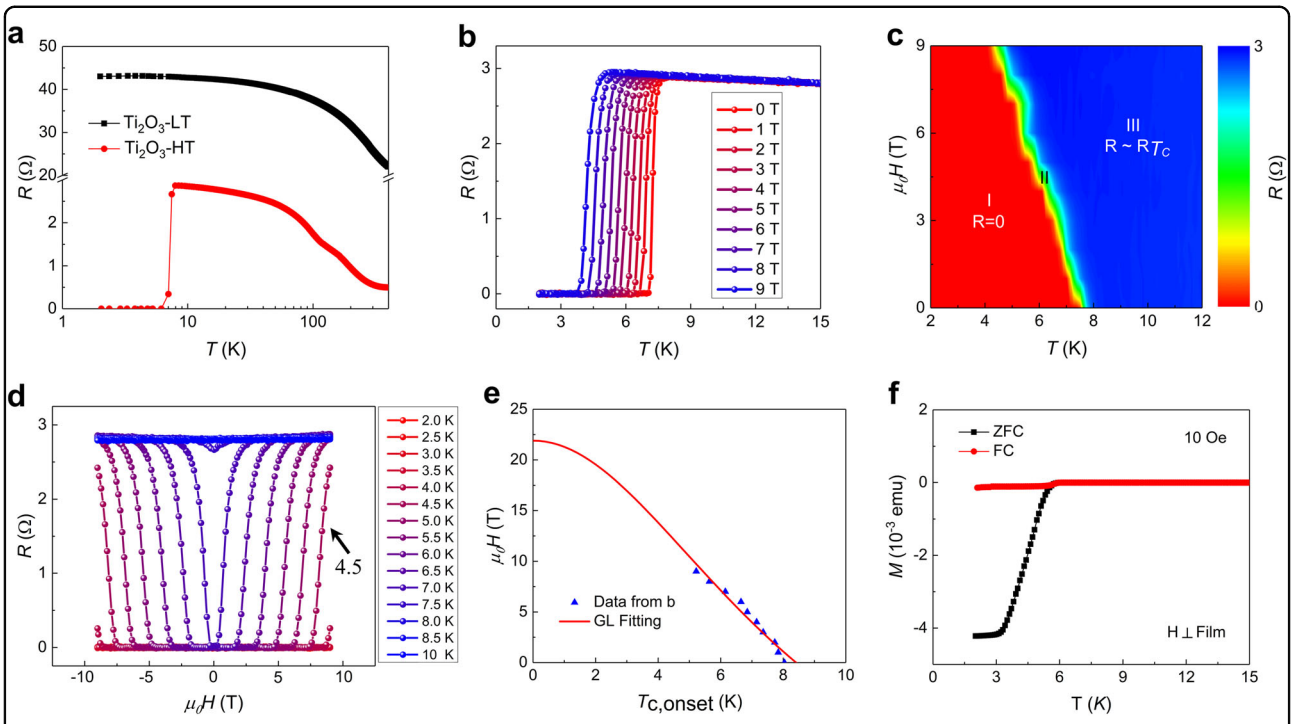

Fig. 6 Superconductivity observed in the orthorhombic-structured Ti_2O_3 polymorph. a Resistance versus temperature data measured on the HT-3 and LT-2 samples. **b** Temperature dependence of the resistance (HT-3) measured under magnetic fields ranging from 0 to 9 T. **c** Superconducting phase diagram in the contour mapping plot using the data in (**b**). **d** Magnetic-field dependence of the resistance measured at fixed temperatures ranging from 2 to 10 K (HT-3). **e** Relationship between the critical magnetic field and the transition temperature. The line is the GL equation fitting. **f** Diamagnetic shielding measurement performed on the HT-3 sample. The temperature dependence of the zero-field-cooling (ZFC) and field-cooling (FC) moment was measured in a field of 10 Oe applied perpendicular to the film surface

Fermi level have contributions from the Ti 3*d* orbitals. More calculated results for Ti_2O_3-LT and Ti_2O_3-HT are shown in Supplementary Figure S17.

Most importantly, the superconductivity of Ti_2O_3 was observed only in the orthorhombic-structured Ti_2O_3 film and not in the corundum-structured bulk phase. Thus, the superconductivity observed in Ti_2O_3 is strongly polymorph-dependent. To our knowledge, only a few materials show polymorph-dependent superconductivity, including tin,[55] zirconium,[56] and $CuSe_2$.[57] For tin, the β-phase (known as white tin) is superconducting, while the α-phase (known as gray tin) tin is semi-metallic. However, a recent breakthrough was made by Liao et al.[58] upon the observation of superconductivity in few-layer stanene (ultrathin α-phase tin). We believe that the exploration of polymorph dependence will attract more interest in the field of superconductor research.

In the current stage, it is difficult for us to identify the mechanism for superconductivity in Ti_2O_3-HT films, which may be different from that in the Cu^{2+} ($3d^9$) and Fe^{2+} ($3d^6$) systems. One unique feature of the orthorhombic-structured Ti_2O_3-HT phase is its high carrier concentration (~10^{22}/cm^3), which is comparable to that of normal superconducting metals.[52] The Bardeen-Cooper-Schrieffer (BCS) theory can describe the quantum-mechanical many-body state of interacting electrons in superconducting metals by considering electron-phonon (*e*-ph) coupling. We calculated the phonon-related properties of unstrained, nonmagnetic Ti_2O_3-HT, and the data for the phonon dispersion, total phonon DOS, and frequency-dependent *e*-ph coupling, $\lambda(\omega)$, are shown in Fig. 7d, e, f, respectively. Remarkably, the total *e*-ph coupling constant, λ, is 1.114, which is large enough to enable electrons to form Cooper pairs (for MgB_2 with $T_C = 40$ K, $\lambda = 0.73$).[59] In contrast, much weaker *e*-ph coupling was obtained for Ti_2O_3-LT (Supplementary Figure S18, $\lambda = 0.46$). The BCS superconducting transition temperature was estimated using the standard Allen-Dynes McMillan equation. As shown in Fig. 7g, using a typical Coulomb pseudopotential, $\mu^* = 0.1$, and electron DOS at the Fermi level, a high T_C above 24 K can be estimated for Ti_2O_3-HT. The deviation between the experimental T_C and the calculation result might be a result of overestimating the electron DOS in the calculation or extrinsic factors such as structural defects and electronic inhomogeneity.

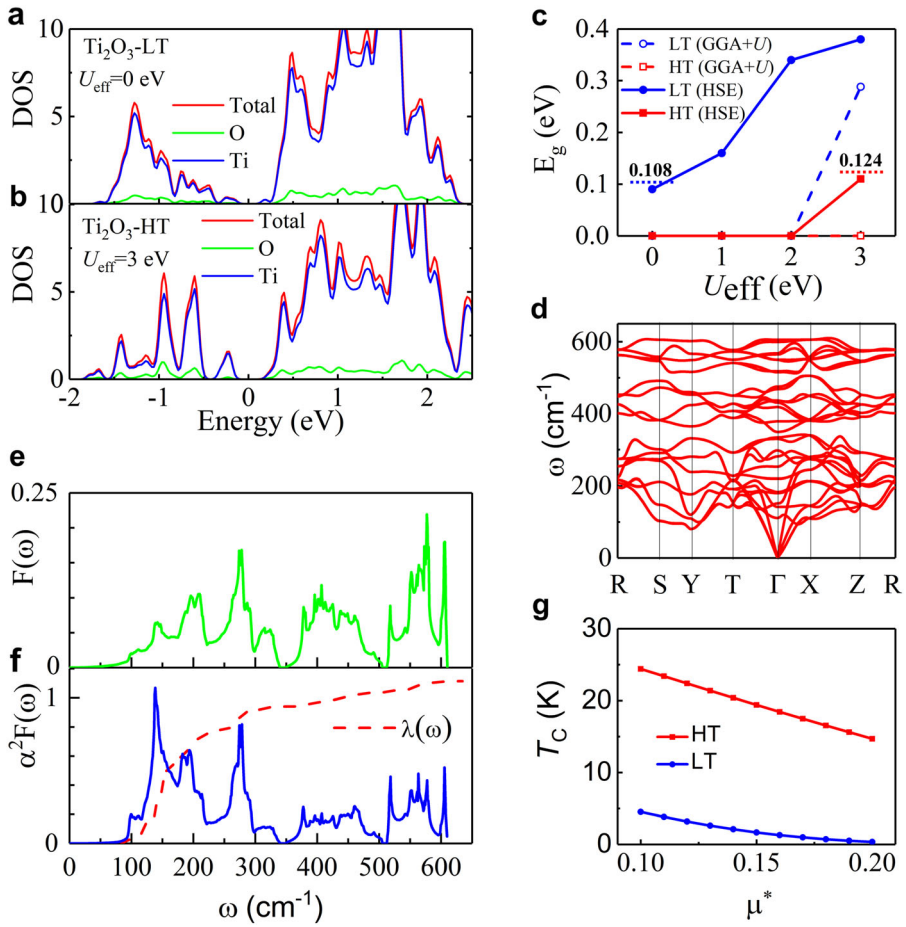

Fig. 7 Theoretical calculations. a, **b** Density of states (DOS) calculated using HSE for Ti_2O_3-LT ($U = 0$ eV) and Ti_2O_3-HT ($U = 3$ eV). **c** Bandgaps calculated using both GGA+U and HSE methods. The HSE method clearly gives a better description of the experimental data. **d** Phonon dispersion spectrum, **e** Total phonon DOS, and **f** Eliashberg function, $\alpha^2F(\omega)$ (solid line), and frequency-dependent electron-phonon coupling, $\lambda(\omega)$ (dashed line), calculated for relaxed Ti_2O_3-HT. **g** T_C of the two Ti_2O_3 phases calculated using different μ^* values

Here, we should note that because of the spin degree of freedom in Ti_2O_3; i.e., Ti ions have a spin of 1/2, superconducting mechanisms beyond the conventional BCS mechanism involving strong quantum fluctuations of magnetism, such as that in the case of cuprates and iron-pnictides/selenides, may play important roles. In fact, if magnetism is considered in the calculation, the ground state is antiferromagnetic for both Ti_2O_3-LT and Ti_2O_3-HT polymorphs (Supplementary Figure S19). Recently, efforts have been devoted to study the interplay between magnetism and superconductivity in cuprates,[60] Fe-based superconductors[61] and 2D oxide interfaces.[62,63] Interestingly, similar to our case, Ti^{3+} has been reported to play an important role in the coexistence of magnetism and superconductivity at the $LaAlO_3/SrTiO_3$ interface.[62,63] Therefore, further studies to elucidate the superconductivity mechanism in orthorhombic-structured Ti_2O_3-HT with $3d^1$ electrons will be interesting and may help boost the T_C in this class of materials.

Conclusion

In summary, we demonstrated the selective stabilization of a new orthorhombic phase of Ti_2O_3 in thin films grown on sapphire substrates. Moreover, as an indication of a strong structure-property correlation, the orthorhombic Ti_2O_3 films showed unexpected superconductivity at 8 K, which is absent in trigonal, corundum-structured Ti_2O_3. Our calculations revealed stronger e-ph coupling in orthorhombic-structured Ti_2O_3 compared to that in the bulk corundum phase. We envision that a further increase in the superconducting temperature could be accomplished by doping and pressure. From the perspective of fundamental science, the discovery of superconductivity in this $3d^1$ electron system may provide a new platform to investigate titanite-based superconductors, which are complementary to the well-explored cuprates ($3d^9$) and iron-based ($3d^6$) systems. Importantly, Ti_2O_3 is earth-abundant, nontoxic and chemically stable, which are essential merits for potential power and communication

applications. Furthermore, our study presents a novel path toward inducing emergent physical phenomena in thin films with newly stabilized polymorph phases, which is promising for advancing material exploration and device technologies.

Acknowledgements
This work is supported by the King Abdullah University of Science and Technology (KAUST). We also acknowledge the National Natural Science Foundation of China (Grant No. 11674055, No.11474146, No. U1532142) and the Hong Kong, Macao and Taiwan Science & Technology Cooperation Program (Grant No. 2015DFH10200).

Author details
[1]Physical Science and Engineering Division, King Abdullah University of Science and Technology (KAUST), Thuwal 23955-6900, Saudi Arabia. [2]Department of Materials Science and Engineering, National University of Singapore, Singapore 117575, Singapore. [3]School of Physics, Southeast University, Nanjing 211189, China. [4]Key Laboratory of Materials Physics, Institute of Solid State Physics, Chinese Academy of Sciences, Hefei 230031, People's Republic of China. [5]Advanced Membranes and Porous Materials Center, Physical Science and Engineering Division, King Abdullah University of Science and Technology (KAUST), Thuwal 23955-6900, Saudi Arabia. [6]Department of Materials Science and Engineering, University of Texas at Dallas, 800 W. Campbell Rd., RL10, Richardson, TX 75080, USA. [7]Advanced Nanofabrication and Imaging Core Laboratory, King Abdullah University of Science and Technology (KAUST), Thuwal 23955-6900, Saudi Arabia. [8]Key Laboratory of Flexible Electronics (KLOFE) & Institute of Advanced Materials (IAM), Jiangsu National Synergetic Innovation Center for Advanced Materials (SICAM), Nanjing Tech University, 30 South Puzhu Road, Nanjing 211816, China. [9]Department of Physics, National University of Singapore, 2 Science Drive 3, Singapore 117542, Singapore. [10]South University of Science and Technology of China, Shenzhen 518055, China. [11]State Key Laboratory of Low-Dimensional Quantum Physics, Department of Physics, Tsinghua University, Beijing 100084, China. [12]Hefei National Laboratory for Physical Sciences at Microscale and Department of Physics, University of Science and Technology of China, Hefei, Anhui 230026, China. [13]School of Materials Science and Engineering, University of New South Wales (UNSW), Sydney, NSW 2052, Australia

Conflict of interest
The authors declare no competing interests.

Supplementary information is available for this paper at https://doi.org/10.1038/s41427-018-0050-5.

Received: 11 November 2017 Revised: 28 February 2018 Accepted: 29 March 2018.
Published online: 6 June 2018

References

1. Wang, J. et al. Epitaxial $BiFeO_3$ multiferroic thin film heterostructures. *Science* **299**, 1719 (2003).
2. Chen, Z. et al. Low-symmetry monoclinic phases and polarization rotation path mediated by epitaxial strain in multiferroic $BiFeO_3$ thin films. *Adv. Funct. Mater.* **21**, 133 (2011).
3. Haeni, J. H. et al. Room-temperature ferroelectricity in strained $SrTiO_3$. *Nature* **430**, 758 (2004).
4. Kim, J. et al. Conversion of an ultra-wide bandgap amorphous oxide insulator to a semiconductor. *NPG Asia Mater.* **9**, e359 (2017).
5. Kleibeuker, J. E. et al. Route to achieving perfect B-site ordering in double perovskite thin films. *NPG Asia Mater.* **9**, e406 (2017).
6. Song, S. et al. Ferroelectric polarization switching with a remarkably high activation energy in orthorhombic $GaFeO_3$ thin films. *NPG Asia Mater.* **8**, e242 (2016).
7. Zeches, R. J. et al. A strain-driven morphotropic phase boundary in $BiFeO_3$. *Science* **326**, 977 (2009).
8. Lee, J. H. et al. Epitaxial stabilization of a new multiferroic hexagonal phase of $TbMnO_3$ thin films. *Adv. Mater.* **18**, 3125 (2006).
9. Wang, J. et al. High-performance photothermal conversion of narrow-bandgap Ti_2O_3 nanoparticles. *Adv. Mater.* **29**, 1603730 (2017).
10. Tsuei, C. C. & Kirtley, J. R. Pairing symmetry in cuprate superconductors. *Rev. Mod. Phys.* **72**, 969 (2000).
11. Schilling, A., Cantoni, M., Guo, J. D. & Ott, H. R. Superconductivity above 130 K in the Hg–Ba–Ca–Cu–O system. *Nature* **363**, 56 (1993).
12. Stewart, G. R. Superconductivity in iron compounds. *Rev. Mod. Phys.* **83**, 1589 (2011).
13. Kamihara, Y., Watanabe, T., Hirano, M. & Hosono, H. Iron-Based Layered Superconductor La[O1-xFx]FeAs (x = 0.05−0.12) with Tc = 26 K. *J. Am. Chem. Soc.* **130**, 3296 (2008).
14. Chen, X. H. et al. Superconductivity at 43 K in SmFeAsO1-xFx. *Nature* **453**, 761 (2008).
15. Wu, G. et al. Superconductivity at 56 K in samarium-doped SrFeAsF. *J. Phys. Condens. Matter* **21**, 142203 (2009).
16. Sweedler, A. R., Raub, Ch. J. & Matthias, B. T. Superconductivity of the alkali tungsten bronzes. *Phys. Lett.* **15**, 108 (1965).
17. Remeika, J. P. et al. Superconductivity in hexagonal tungsten bronzes. *Phys. Lett.* **24A**, 565 (1967).
18. Uchida, Shin-ichi. *High Temperature Superconductivity*. 89–92 (Springer: Japan, 2015).
19. Schooley, J. F., Hosler, W. R. & Cohen, M. L. Superconductivity in semiconducting $SrTiO_3$. *Phys. Rev. Lett.* **12**, 474 (1964).
20. Reed, T. B., Banus, M. D., Sjöstrand, M. & Keesom, P. H. Superconductivity in cubic and monoclinic "TiO". *J. Appl. Phys.* **43**, 2478 (1972).
21. Doyle, N. J., Hulm, J. K., Jones, C. K., Miller, R. C. & Taylor, A. Vacancies and superconductivity in titanium monoxide. *Phys. Lett.* **26A**, 604 (1968).
22. Johnston, D. C., Prakash, H., Zzchariasen, W. H. & Viswanathan, R. High temperature superconductivity in the Li-Ti-O ternary system. *Mat. Res. Bull.* **8**, 777 (1973).
23. Johnston, D. C. Superconducting and normal state properties of $Li_{1+x}Ti_{2-x}O_4$ spinel compounds. I. Preparation, crystallography, superconducting properties, electrical resistivity, dielectric behavior, and magnetic susceptibility. *J. Low. Temp. Phys.* **25**, 145 (1976).
24. Satpathy, S. & Martin, R. M. Electronic structure of the superconducting oxide spinel $LiTi_2O_4$. *Phys. Rev. B* **36**, 7269 (1987).
25. Zhang, C. et al. Enhanced superconductivity in TiO epitaxial thin films. *npj Quantum Mater.* **2**, 2 (2017).
26. Kurokawa, H., Yoshimatsu, K., Sakata, O. & Ohtomo, A. Effects of phase fraction on superconductivity of low-valence eutectic titanate films. *J. Appl. Phys.* **122**, 055302 (2017).
27. Yoshimatsu, K., Sakata, O. & Ohtomo, A. Superconductivity in Ti_4O_7 and γ-Ti_3O_5 films. *Sci. Rep.* **7**, 12544 (2017).
28. Hulm, J. K., Jones, C. K., Hein, R. A. & Gibson, J. W. Superconductivity in the TiO and NbO systems. *J. Low. Temp. Phys.* **7**, 291 (1972).
29. Makise, K. et al. Superconductivity in transparent zinc-doped In_2O_3 films having low carrier density. *Sci. Technol. Adv. Mater.* **9**, 044208 (2008).
30. Mori, N. Superconductivity in transparent Sn-doped In_2O_3 films. *J. Appl. Phys.* **73**, 1327 (1993).
31. Ge, J. F. et al. Superconductivity above 100 K in single-layer FeSe films on doped $SrTiO_3$. *Nat. Mater.* **14**, 285 (2015).
32. Hsu, F. C. et al. Superconductivity in the PbO-type structure α-FeSe. *Proc. Natl. Acad. Sci. USA* **105**, 14262 (2008).
33. Ovsyannikov, S. V. et al. Structural stability of a golden semiconducting orthorhombic polymorph of Ti_2O_3 under high pressures and high temperatures. *J. Phys. Condens. Matter* **22**, 375402 (2010).
34. Perdew, J. P. et al. Restoring the density-gradient expansion for exchange in solids and surfaces. *Phys. Rev. Lett.* **100**, 136406 (2008).
35. Kresse, G. & Hafner, J. Ab initio molecular dynamics for liquid metals. *Phys. Rev. B* **47**, 558 (1993).
36. Kresse, G. & Furthmüller, J. Efficient iterative schemes for ab initio total-energy calculations using a plane-wave basis set. *Phys. Rev. B* **54**, 11169 (1996).
37. Heyd, J., Scuseria, G. E. & Ernzerhof, M. Hybrid functionals based on a screened Coulomb potential. *J. Chem. Phys.* **118**, 8207 (2003).

38. Giannozzi, P. et al. QUANTUM ESPRESSO: a modular and open-source software project for quantum simulations of materials. *J. Phys. Condens. Matter* **21**, 395502 (2009).
39. Mooradian, A. & Raccah, P. M. Raman study of the semiconductor-metal transition in Ti_2O_3. *Phys. Rev. B* **3**, 4253 (1971).
40. Kurtz, R. L. & Henrich, V. E. UHV-cleaved single crystal Ti_2O_3 ($10\bar{1}2$) by UPS and XPS. *Surf. Sci. Spectra* **5**, 182 (1998).
41. Kurtz, R. L. & Henrich, V. E. Comparison of Ti 2p core-level peaks from TiO_2, Ti_2O_3, and Ti metal, by XPS. *Surf. Sci. Spectra* **5**, 179 (1998).
42. Shen, Z. et al. Stabilization of microcrystal λ—Ti_3O_5 at room temperature by aluminum-ion doping. *Appl. Phys. Lett.* **111**, 191902 (2017).
43. Li, Y. et al. Orthorhombic Ti_2O_3: a polymorph-dependent narrow-bandgap ferromagnetic oxide. *Adv. Funct. Mater.* **28**, 1705657 (2018).
44. Li, Y. et al. Nanoscale chemical and valence evolution at the metal/oxide interface: a case study of Ti/$SrTiO_3$. *Adv. Mater. Interfaces* **3**, 1600201 (2016).
45. Han, K. et al. Controlling Kondo-like scattering at the $SrTiO_3$-based Interfaces. *Sci. Rep.* **6**, 25455 (2016).
46. Zeng, X. et al. In situ epitaxial MgB_2 thin films for superconducting electronics. *Nat. Mater.* **1**, 35 (2002).
47. Takahashi, N. et al. Fabrication of epitaxial Fe_3O_4 film on a Si(111) substrate. *Sci. Rep.* **7**, 7009 (2017).
48. Wang, W. et al. Control of interfacial reactions for the growth of high-quality AlN epitaxial films on Cu(111) substrates. *CrystEngComm* **19**, 7307 (2017).
49. Kim, Y. et al. Elastic strain relief in nitridated Ga metal buffer layers for epitaxial GaN growth. *Appl. Phys. Lett.* **78**, 895 (2001).
50. Morin, F. J. Oxides which show a metal-to-insulator transition at the Neel Temperature. *Phys. Rev. Lett.* **3**, 34 (1959).
51. Yahia, J. & Frederikse, H. P. R. Electrical conduction in p-Type titanium sesquioxide. *Phys. Rev.* **123**, 1257 (1961).
52. Malliakas, C. D., Chung, D. Y., Claus, H. & Kanatzidis, M. G. Superconductivity in the narrow-gap semiconductor $CsBi_4Te_6$. *J. Am. Chem. Soc.* **135**, 14540 (2013).
53. Zhou, H. D. & Goodenough, J. B. Semiconductor-semiconductor transition in $Mg[Ti_2]O_4$. *Phys. Rev. B* **72**, 045118 (2005).
54. Tang, Z. T. et al. Unconventional superconductivity in quasi-one-dimensional $Rb_2Cr_3As_3$. *Phys. Rev. B* **91**, 020506(R) (2015).
55. Wang, K. J. & Cohen, M. L. Electron–phonon interactions and superconductivity in Si, Ge, and Sn. *Phys. Rev. B* **34**, 4552–4557 (1986).
56. Tittmann, B., Hamilton, D. & Jayaraman, A. Superconducting behaviour of pressure-induced zirconium polymorph. *J. Appl. Phys.* **35**, 732 (1964).
57. Martinolich, A. J., Kurzman, J. A. & Neilson, J. R. Polymorph selectivity of superconducting $CuSe_2$ through kinetic control of solid-state metathesis. *J. Am. Chem. Soc.* **137**, 3827–3833 (2015).
58. Liao, M. *et al*. Superconductivity in few-layer stanene. *Nat. Phys*. https://doi.org/10.1038/s41567-017-0031-6 (2018).
59. Bohnen, K. P., Heid, R. & Renker, B. Phonon dispersion and electron-phonon coupling in MgB_2 and AlB_2. *Phys. Rev. Lett.* **86**, 5771 (2001).
60. Crisan, A. et al. Coexistence of superconductivity and antiferromagnetism in $HgBa_2Ca_4Cu_5O_y$: multiharmonic susceptibility and vortex dynamics study. *Phys. Rev. B* **76**, 212508 (2007).
61. Shermadini, Z. et al. Coexistence of magnetism and superconductivity in the iron-based compound $Cs_{0.8}(FeSe_{0.98})_2$. *Phys. Rev. Lett.* **106**, 117602 (2011).
62. Bert, J. A. et al. Direct imaging of the coexistence of ferromagnetism and superconductivity at the $LaAlO_3/SrTiO_3$interface. *Nat. Phys.* **7**, 767–771 (2011).
63. Dikin, D. A. et al. Coexistence of superconductivity and ferromagnetism in two dimensions. *Phys. Rev. Lett.* **107**, 056802 (2011).